Available online at www.sciencedirect.com
ScienceDirect
Journal of Power Sources 170 (2007) 150–159
JOURNAL OF POWER SOURCES
www.elsevier.com/locate/jpowsour

1 kW_e sodium borohydride hydrogen generation system Part II: Reactor modeling

Jinsong Zhang, Yuan Zheng *, Jay P. Gore, Issam Mudawar, T.S. Fisher

School of Mechanical Engineering, The Energy Center at Discovery Park, Purdue University, West Lafayette, IN 47907-2088, USA

Received 15 January 2007; received in revised form 7 March 2007; accepted 8 March 2007
Available online 15 March 2007

Abstract

Sodium borohydride ($NaBH_4$) hydrogen storage systems offer many advantages for hydrogen storage applications. The physical processes inside a $NaBH_4$ packed bed reactor involve multi-component and multi-phase flow and multi-mode heat and mass transfer. These processes are also coupled with reaction kinetics. To guide reactor design and optimization, a reactor model involving all of these processes is desired. A one-dimensional numerical model in conjunction with the assumption of homogeneous catalysis is developed in this study. Two submodels have been created to simulate non-isothermal water evaporation processes and pressure drop of two-phase flow through the porous medium. The diffusion coefficient of liquid inside the porous catalyst pellets and the mass transfer coefficient of water vapor are estimated by fitting experimental data at one specified condition and have been verified at other conditions. The predicted temperature profiles, fuel conversion, relative humidity and pressure drops match experimental data reasonably well.

Keywords: Sodium borohydride; Reactor modeling; Porous media; Multi-phase

1. Introduction

A sodium borohydride hydrogen generator is unique because both reactants can be stored together, and hydrogen is generated by passing sodium borohydride solution through a catalyst bed to initiate hydrolysis reaction as [1]:

$$NaBH_4 + 2H_2O \xrightarrow{\text{Catalyst}} NaBO_2 + 4H_2 + \text{Heat} \quad (1)$$

The effects of catalysts, pH and temperature on sodium borohydride hydrolysis reaction were discussed in Ref. [2]. Our experimental paper [3] discussed system-level experiments on a 1 kW_e sodium borohydride hydrogen generator and exposes solubility issues that may limit the maximum usable concentration to approximately 15%, which may preclude automotive applications; nevertheless, sodium borohydride systems may still find applications in portable electronic devices and other niche areas [4,5]. Most prior work on sodium borohydride systems has focused on experimental testing, and no work on system-level reactor modeling has been reported to date. The processes in the reactor are quite complex, involving multiple components ($NaBH_4$, NaOH, $NaBO_2$, H_2O, H_2) and multiple phases (liquid and gas). In addition, general liquid phase reactions inside a packed bed reactor accompanied by significant water evaporation have not received attention in the literature. As a result, a significant need exists for a sodium borohydride hydrolysis reactor model to enable reactor design and optimization. The development of such a reactor model will also facilitate the study of hydrogen storage systems using other chemical hydrides. Thus motivated, we have developed a one-dimensional numerical model in conjunction with the assumption of homogeneous catalysis and have validated this model with experimental data.

2. Experiments

A 1 kW_e sodium borohydride hydrogen generation system (by assuming a fuel cell efficiency of 50%) has been established for system-level studies. The 1 kW_e hydrogen generation apparatus was described in detail in a previous paper [3] and is only summarized here. Fig. 1 shows the section view of the

* Corresponding author. Tel.: +1 765 494 0061; fax: +1 765 494 0530.
E-mail address: zhengy@ecn.purdue.edu (Y. Zheng).

0378-7753/$ – see front matter © 2007 Elsevier B.V. All rights reserved.
doi:10.1016/j.jpowsour.2007.03.025

Nomenclature

a_g external surface area per volume of catalytic bed ($m^2\ m^{-3}$) $= 6(1-\varepsilon)/d_p$ for packed bed ($m^2\ m^{-3}$)
A_t cross-sectional area of the reactor (m^2)
$c_{p,f}$ specific heat of the fuel ($kJ\ kg^{-1}\ k^{-1}$)
C_A molar concentration of species A in the fluid ($kmol\ m_f^{-3}$)
d_p particle diameter, equivalent diameter of sphere of the same external surface area (m)
d_t internal tube diameter of the reactor (m_r)
$D_{l,A,e}$ effective liquid diffusivity inside the catalyst at temperature T ($m_f^3\ m_p^{-1}\ s^{-1}$)
$D_{l,A}$ liquid diffusivity inside the catalyst at temperature T ($m_f^3\ m_p^{-1}\ s^{-1}$)
$D_{l,A,0}$ liquid diffusivity inside the catalyst at temperature T_0 ($m_f^3\ m_p^{-1}\ s^{-1}$)
E_{act} activation energy for sodium borohydride hydrolysis on ruthenium catalyst (66,900 kJ $kmol^{-1}$)
f_{TP} two-phase factor (2.3 was used in current study)
h_{fg} heat of vaporization of water, assumed to be constant 2250 kJ kg^{-1} or 40,500 kJ $kmol^{-1}$
ΔH_{ads} heat of reaction for the adsorption of borohydride ion on the surface of ruthenium catalyst (−35,000 kJ $kmol^{-1}$)
ΔH_{rxn} heat of reaction for the sodium borohydride hydrolysis (−210,000 kJ $kmol^{-1}$)
k_L reaction rate coefficient for Langmuire–Hinshelwood kinetic model ($kmol\ kg\ cat^{-1}\ s^{-1}$)
k_l mass transfer coefficient from liquid to solid interface, based on concentration driving force ($m_f^3\ m_i^{-2}\ s^{-1}$)
k_{H_2O} mass transfer coefficient for water vapor (m^{-1})
K isotherm adsorption coefficient for borohydride ion on the surface of the catalyst ($m^3\ kmol^{-1}$)
L length of the reactor (m)
$\dot{m}_f$ mass flow rate of sodium borohydride solution ($kg\ s^{-1}$)
$\dot{m}_{f,0}$ initial mass flow rate of sodium borohydride solution ($kg\ s^{-1}$)
MW_{H_2} molecular weight of hydrogen ($kg\ kmol^{-1}$)
MW_{H_2O} molecular weight of water ($kg\ kmol^{-1}$)
$\dot{n}_B$ molar flow rate of liquid water ($kmol\ s^{-1}$)
$\dot{n}_C$ molar flow rate of hydrogen ($kmol\ s^{-1}$)
$\dot{n}_D$ molar flow rate of water vapor carried with hydrogen stream ($kmol\ s^{-1}$)
n'_{evap} total rate of water vaporization per unit catalyst mass (kmol water $kg\ cat^{-1}\ s^{-1}$)
$n'_{evap,1}$ rate of water vaporization corresponding to the generation of hydrogen per unit catalyst mass (kmol water $kg\ cat^{-1}\ s^{-1}$)
$n'_{evap,2}$ rate of water vaporization corresponding to mass transfer from catalyst surface to the bulk gas stream per unit catalyst mass (kmol water $kg\ cat^{-1}\ s^{-1}$)
P_{back} backpressure of the reactor (bar)
$P_{sat,H_2O}(T)$ saturation pressure of water vapor at temperature T (bar)
P_t total pressure of the reactor at location z (bar)
ΔP_{fritz} total pressure drop across the fritzs (Pa, psi)
ΔP_{total} total pressure drop across the reactor (Pa, psi)
r'_A rate of reaction per unit catalyst mass ($kmol\ kg\ cat^{-1}\ s^{-1}$)
$Re_l = d_p \rho_l u_s / \mu_l$ Reynolds number of the liquid phase
R universal gas constant, 8.314 (kJ $kmol^{-1}\ K^{-1}$)
RH relative humidity of hydrogen stream
S_{pellet} the external surface area of the pellet (m^2)
T temperature in the reactor at location z (K)
T_∞ ambient temperature (K)
$u_{l,s}$ superficial velocity of the liquid phase through the bed ($m\ s^{-1}$)
$u_{g,s}$ superficial velocity of the gaseous phase ($m\ s^{-1}$)
$\bar{u}$ average velocity of the multi-phase fluid across the reactor ($m\ s^{-1}$)
$\dot{V}_g$ volumetric flow rate of the gaseous phase (m^3)
V_{pellet} the volume of the pellet (m^3)
W_f total mass flow rate of the liquid phase ($kg\ s^{-1}$)
W_g total mass flow rate of the gas phase ($kg\ s^{-1}$)
W_{total} total mass flow rate of the multi-phase fluid ($kg\ s^{-1}$)
x_A conversion of sodium borohydride
$x_{quality}$ fraction of the gas phase out of the multi-phase fluid
z axial direction (m)

Greek letters

ε void fraction of packing in a packed bed ($m_f^3\ m_r^{-3}$)
ε_s internal void fraction of the catalyst pellet, between 0.3 and 0.8, typically 0.40
ϕ thiele modulus number for cylinder
η_G overall effectiveness factor
η effectiveness factor
μ_l liquid viscosity at temperature T ($kg\ m^{-1}\ s^{-1}$)
$\mu_{l,0}$ liquid viscosity at temperature T_0 ($kg\ m^{-1}\ s^{-1}$)
ρ_b catalyst bulk density in a packed bed ($kg\ m^{-3}$)
ρ_f fluid density ($kg\ m^{-3}$)
ρ_g density of the gaseous phase ($kg\ m^{-3}$)
ρ_s density of catalyst ($kg\ cat\ m_p^{-3}$)
ρ_{H_2} density of the hydrogen gas ($kg\ m^{-3}$)
$\rho_{H_2O\ vapor}$ density of the water vapor ($kg\ m^{-3}$)
$\bar{\rho}$ weighted average density of the multi-phase fluid ($kg\ m^{-3}$)
τ tortuosity factor, typically 3.0 to 4.0

Subscripts

0 initial condition
A sodium borohydride
b bulk phase
B liquid water
C hydrogen

D	water vapor
f	liquid phase
g	gaseous phase
l	liquid phase
s	catalyst
s	superficial
t	total

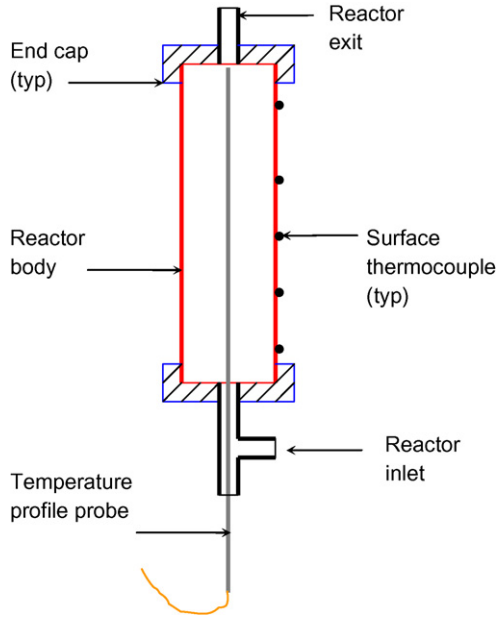

Fig. 1. Section view of the reactor.

stainless steel reactor. A distinct feature of this reactor is its stainless steel temperature profile probe, which enables accurate measurement of temperature profiles inside the reactor. The locations of all thermocouples (designated as PT-#) from the inlet are listed in Table 1. The inner diameter of the reactor was 2.09 cm, and the height of the reactor was 28.7 cm. The wall thickness of the reactor was 2.9 mm. The reactor had an internal volume of 98 mL. The catalyst used was 3% 2 mm Ru on carbon extrudate (Johnson Matthey). The total catalyst mass was 55.9 g, and the catalyst bed density was therefore 570 kg m^{-3}. At the inlet, a stainless steel fritz was used to retain the catalyst and to distribute inlet flow. At the outlet, another stainless steel fritz was used to retain the catalyst. To simplify the physical model for reactor modeling, the reactor was thermally insulated during experiments to simulate adiabatic operation conditions. All downstream tubing and devices were also insulated for the same purpose.

Table 1
Axial locations of thermocouples from the bottom of the reactor

Name	Distance from the inlet (cm)
PT-1	28.70
PT-2	25.53
PT-3	22.35
PT-4	19.18
PT-5	16.00
PT-6	12.83
PT-7	9.65
PT-8	6.48
PT-9	3.30
PT-10	0.13

Tests were conducted at different fuel solution flow rates, operating pressures and inlet temperatures. The fuel concentrations used were 5%, 10%, 15% and 20%. The concentration of NaOH (stabilizer) in all solutions was 3% and the pH of all solutions was 14 [6,7]. The accuracy of temperature measurements was within ±0.5 °C. Relative humidity was measured indirectly by condensing the hydrogen stream using a plate heat exchanger and measuring the weight of the condensate. The uncertainty of relative humidity is approximately ±10% [3]. Conversion of $NaBH_4$ was measured using two methods. The first involved measuring the amount of hydrogen gas evolved from acid-catalyzed hydrolysis of the product liquid. The second method involved measuring the flow rate of hydrogen generated using a flowmeter and comparing it to that based on the measured fuel inflow rate and 100% conversion. The two methods were found to match each other quite well, typically within 5%; as a result, only the second method was used for later experiments because it was easier to implement.

3. Modeling

3.1. Physical processes inside the reactor

At the reactor's entrance, liquid phase $NaBH_4$ solution (reactants) is introduced from the bottom of the catalyst bed. Then, the catalyst initiated hydrolysis that heats the reactants and the catalyst bed. The increase in reactor temperature along the flow path increases the reaction rate significantly. Because the reaction is exothermic (−210,000 kJ $kmol^{-1}$), water vaporized along with hydrogen generation. Throughout the catalyst bed, the flow is multi-phase (liquid and gas) and multi-component ($NaBH_4$, NaOH, $NaBO_2$, H_2O, H_2). Heat transfer involves convection and conduction, in addition to the heat conduction inside the catalyst pellets. All heat transfer processes are closely coupled with mass transfer processes (e.g., diffusion of $NaBH_4$ into the pores of the catalyst pellets) and chemical kinetics; and detailed modeling of all processes in the catalyst bed is therefore challenging. This work reports a foundational effort in solving this complicated problem.

The present model assumes that the catalyst is homogeneously distributed inside the reactor, and that the reactor conditions vary in axial direction only and are uniform in each cross-section. For modeling purposes, the catalyst only affects the results through the void fraction of the catalyst bed. The kinetic model assumes uniform concentration and temperature at each cross-section and employs an overall effectiveness factor. The overall effectiveness factor accounts for both the external mass transfer coefficient outside the catalyst pellet and internal diffusion effects inside the catalyst pellet. A schematic of the model is shown in Fig. 2.

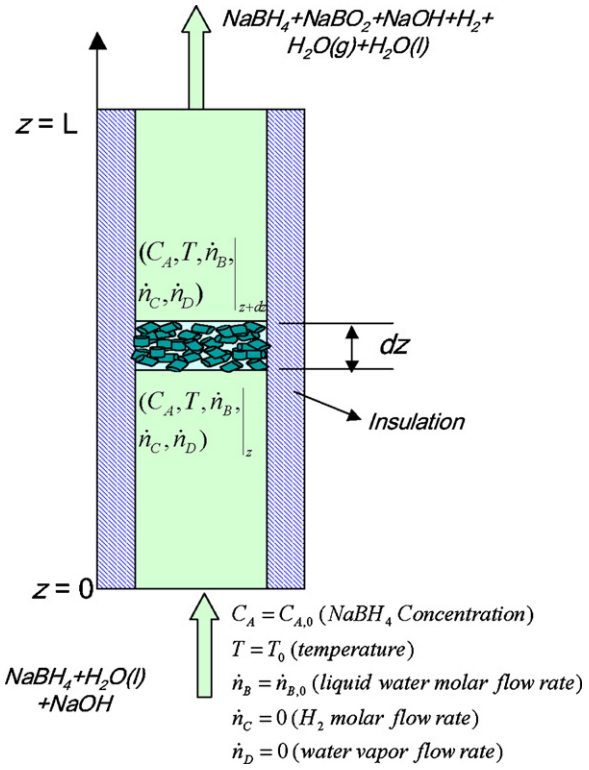

Fig. 2. Schematic of the homogeneous model.

3.2. Governing equations

The concentration of component A ($NaBH_4$) satisfies a steady-state continuity equation [8] (for simplicity, axial diffusion is ignored):

$$u_{l,s}\frac{dC_A}{dz} = r'_A\rho_b \tag{2}$$

where,

$$u_{l,s} = \frac{\dot{m}_f}{\rho_f A_t} \tag{3}$$

$$\rho_f = \rho_{f,0}(1 - x_A) - \rho_{f,f}x_A \tag{4}$$

$$x_A = 1 - \frac{C_A}{C_{A,0}} \tag{5}$$

$$\dot{m}_f = \dot{m}_{f,0} - \dot{n}_C MW_{H_2} - \dot{n}_D MW_{H_2O} \tag{6}$$

For other components, a molar flow rate approach is used. The steady-state continuity equations for component B (liquid water), component C (hydrogen) and component D (water vapor) can be written as:

$$\frac{d\dot{n}_B}{dz} = (2r'_A\rho_b - n'_{evap}\rho_b)A_t \tag{7}$$

$$\frac{d\dot{n}_C}{dz} = -4r'_A\rho_b A_t \tag{8}$$

$$\frac{d\dot{n}_D}{dz} = n'_{evap}\rho_b A_t \tag{9}$$

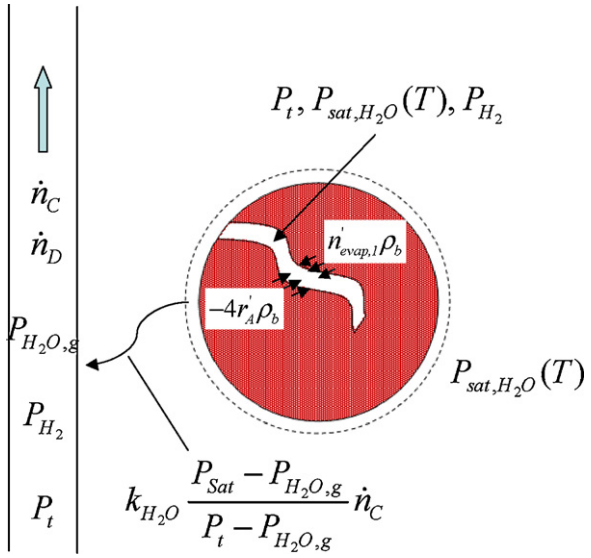

Fig. 3. Schematic of water vapor generation inside a catalyst pellet and water transport in the bulk space.

where,

$$n'_{evap} = n'_{evap,1} + n'_{evap,2} \tag{10}$$

Eq. (8) for hydrogen is based on reaction stoichiometrics. The negative sign is present because the rate of reaction is defined based on the consumption of $NaBH_4$.

Modeling water vapor generation described in Eq. (10) is difficult because water vaporizes at different temperatures and locations in the reactor, in contrast to the isothermal conditions for most boiling situations [9]. Initially we assumed that water vapor generation is associated only with hydrogen generation and that hydrogen generated in each spanwise control volume was saturated with water vapor at the local temperature because hydrogen is generated from small pores inside the catalyst support, as shown in Fig. 3. As a result, the partial pressure of the water vapor carried by the hydrogen would be the saturated water vapor pressure at that temperature. Therefore, according to Dalton's law:

$$\frac{-4r'_A\rho_b}{n'_{evap,1}\rho_b} = \frac{P_t - P_{sat,H_2O}(T)}{P_{sat,H_2O}(T)} \tag{11}$$

The preliminary simulation results indicated that the predicted relative humidity as defined below, of the exiting hydrogen stream was significantly lower than measured data.

$$RH = \frac{P_{H_2O,g}}{P_{Sat,H_2O(T)}} \tag{12}$$

Therefore, the previous assumption was modified. Because of the large temperature variation inside the reactor, saturated hydrogen gas generated in the lower part of the reactor becomes unsaturated when it passes through the upper part of the reactor. Mass transfer of water from the liquid phase to the bulk gas stream should also be included. Mass transfer rates increase with an increase in driving potential ($P_{Sat} - P_{H_2O,g}$) and with the molar flow rate of the gas stream. As a result, we account

for additional mass transfer of water from the liquid phase to the bulk gas stream by relating it to the hydrogen molar flow rate.

$$n'_{\text{evap},2} = \frac{k_{H_2O}}{\rho_b A_t} \frac{P_{Sat} - P_{H_2O,g}}{P_t - P_{H_2O,g}} \dot{n}_C \tag{13}$$

The denominator is used to convert the pressure-based driving potential to a molar flow rate-based driving potential using Dalton's Law, similar to Eq. (11). The mass transfer coefficient for water k_{H_2O} is not available in the literature and was estimated by varying its value to match one set of the experimental data as described in Section 4.1. In the calculations, P_t is assumed to equal to the measured pressure head at the entrance of the reactor and remains constant throughout the reactor.

Because the reactor was thermally insulated during experiments, the reactor is assumed to be adiabatic, and heat loss from the reactor to the ambient has been ignored. Therefore, the energy equation can be written as [8]:

$$\left(\rho_f u_{l,s} c_{p,f} + \frac{\dot{n}_C MW_{H_2} c_{p,H_2} + \dot{n}_D MW_{H_2O} c_{p,H_2O}}{A_t}\right) \frac{dT}{dz} = \Delta H_{rxn} r'_A \rho_b - h_{fg} n'_{evap} \rho_b \tag{14}$$

To predict the pressure drop of multi-component, multi-phase flow through a porous medium, a homogeneous equilibrium model (HEM) from two-phase flow theory [10] may be used assuming that the liquid and gas phases have the same velocity. The total pressure gradient consists of three components (accelerational, gravitational and frictional) that can be calculated as:

$$\left.\frac{dp}{dz}\right|_{\text{total}} = \left.\frac{dp}{dz}\right|_{\text{accelerational}} + \left.\frac{dp}{dz}\right|_{\text{gravitational}} + \left.\frac{dp}{dz}\right|_{\text{frictional}} \tag{15}$$

$$\left.\frac{dp}{dz}\right|_{\text{accelerational}} = \frac{W_{\text{total}}}{A_t} \frac{d\bar{u}}{dz} \tag{16}$$

$$\left.\frac{dp}{dz}\right|_{\text{gravitational}} = \bar{\rho} g \tag{17}$$

where,

$$\bar{u} = \frac{W_{\text{total}}}{\bar{\rho} A_t \varepsilon} \tag{18}$$

$$W_{\text{total}} = W_g + W_f \tag{19}$$

$$W_f = \dot{m}_{f,0} - \dot{n}_C MW_{H_2} - \dot{n}_D MW_{H_2O} \tag{20}$$

$$W_g = \dot{n}_C MW_{H_2} + \dot{n}_D MW_{H_2} \tag{21}$$

$$x_{\text{quality}} = \frac{W_g}{W_g + W_f} \tag{22}$$

$$\bar{\rho} = \frac{1}{(x_{\text{quality}}/\rho_g) + (1 - x_{\text{quality}}/\rho_f)} \tag{23}$$

$$\rho_g = \frac{\dot{n}_C \rho_{H_2} + \dot{n}_D \rho_{H_2O\,\text{vapor}}}{\dot{n}_C + \dot{n}_D} \tag{24}$$

For the frictional pressure gradient term in Eq. (15), no correlation is available for multi-phase flow through porous media; therefore, we propose the following formula based on single-phase flow through porous media [8] and two-phase flow theories [10].

$$\left.\frac{dp}{dz}\right|_{\text{frictional}} = 2 f_{TP} \bar{\rho} \frac{\bar{u}^2}{d_p} \tag{25}$$

The equivalent diameter d_p of the catalyst pellet (the diameter when the external surface area of the sphere equals that of non-spherical particles [11]) was used here instead of the reactor diameter d_t to account for the porous-media flow and a two-phase factor f_{TP} was used to account for two-phase phenomena. We found that $f_{TP} = 2.3$ resulted in a good match with experimental data.

To calculate the total pressure drop across the reactor, the pressure drop across both fritzes (ΔP_{fritz}) is determined by a correlation provided by the manufacturer. The total pressure drop can then be calculated as:

$$\Delta P_{\text{total}} = \int_0^L \left.\frac{dP}{dz}\right|_{\text{total}} dz + \Delta P_{\text{fritz}} \tag{26}$$

The entrance ($z = 0$) boundary conditions for the foregoing continuity, energy and momentum equations are:

$$C_A = C_{A,0} \tag{27}$$

$$T = T_0 \tag{28}$$

$$\dot{n}_B = \dot{n}_{B,0} \tag{29}$$

$$\dot{n}_C = 0 \tag{30}$$

$$\dot{n}_D = 0 \tag{31}$$

Chemical reactions are modeled using the Langmuir–Hinshelwood kinetic model developed in reference [2]. To account for the diffusion of reactants from the catalyst surface to the interior of the catalyst pellet, an effectiveness factor has been employed. The effectiveness factor calculation for a Langmuir–Hinshelwood kinetic model is quite complicated, and most prior results [12–14] have been presented on a log–log scale, making an integrated computer model difficult to implement. As a result, we have used the general modulus and corresponding effectiveness factor expression proposed by Hong et al. [15]. The proposed modulus approximates the standard modulus to within 5%. To consider both the effects of mass transfer resistance from the bulk liquid phase to the surface of the catalyst pellet and internal diffusion effects, an overall effectiveness factor was used [11]. The primary equations for chemical kinetics are:

$$r'_A = -\eta_G k_L \frac{K C_A}{1 + K C_A} \tag{32}$$

$$k_L = A e^{-E_{act}/RT} \tag{33}$$

$$K = 1.6 \times 10^{-4} \exp\left(-\frac{\Delta H_{ads}}{RT}\right) \tag{34}$$

$$\eta_G = \frac{1}{(1/\eta) + (k_L K \rho_s / k_l a_g)} \quad (35)$$

$$\eta = \frac{1}{\phi}\left(\frac{1}{\tanh(3\phi)} - \frac{1}{3\phi}\right) \quad (36)$$

$$\phi = \frac{V_{pellet}}{S_{pellet}}\sqrt{\frac{k_L K \rho_s}{D_{l,A,e}(2KC_A + (1/(1+KC_A)))}} \quad (37)$$

According to reference [2], the pre-exponential factor A in Eq. (33) is $e^{16.903}$ kmol s^{-1} kgcat., and the activation energy is 66,900 kJ kmol^{-1}. ΔH_{ads} in Eq. (34) is $-35{,}000$ kJ kmol^{-1}.

Two variables, the tortuosity factor τ and internal void fraction ε_s, are needed to calculate the effective diffusivity ($D_{l,A,e}$) of liquid inside the pores [8]. These factors account for the porosity of the catalyst support and the fact that the characteristic diffusion path length through the pores is greater than the measurable pellet thickness due to the tortuous nature of the pores and the pore constrictions. According to the recommendation of Satterfield [16], we have used a tortuosity factor of 4.0 and a void fraction of 0.4. The effective diffusion coefficient of liquid inside the pores is thus calculated from the intrinsic diffusion coefficient as:

$$D_{l,A,e} = \frac{D_{l,A}\varepsilon_s}{\tau} \quad (38)$$

To account for the significant variation of diffusivity with temperature, the following approximation has been adopted [11]:

$$D_{l,A} = D_{l,A,0}\frac{\mu_{l,0}}{\mu_l}\frac{T}{T_0} \quad (39)$$

Dwidevi and Upadhyay [17] have developed a mass transfer coefficient model that is valid for both gases ($Re > 10$) and liquids ($Re > 0.01$) in either fixed or fluidized beds. However, the mass transfer coefficient calculated using this model is of the order of 10^{-6} m s^{-1}, which is much smaller than mass transfer coefficients reported for similar conditions [11]. The correlations may not be applicable to multi-phase flow, which exists in our study. Because the generation rate is so much larger than the liquid flow rate, the actual mass transfer coefficient should be much larger. As a result, we have used a typical mass transfer coefficient value $k_l = 2.0$ m s^{-1} [11] and found that under this assumption, the overall effectiveness factor equals the internal effectiveness factor, indicating that the reaction is limited by internal diffusion.

Eqs. (2)–(39) have been assembled and solved iteratively using Engineering-Equations Solver (EES) software [18]. The numerical integration grid spacing was 0.0005 m in all calculations. Reducing the spacing further did not affect the results.

4. Results and discussion

4.1. Model parameters

Both the diffusion coefficient $D_{l,A,0}$ and the water vapor mass transfer coefficient k_{H_2O} were adjusted to fit experimental data at a moderate flow rate ($\dot{m}_{f,0} = 48.5$ g min^{-1}) for 10% $NaBH_4$. The density of the 10% $NaBH_4$ solution has been measured to be 1045 kg m^{-3}, and the density of the corresponding discharge solution has been measured to be 1200 kg m^{-3}. The specific heat of the liquid phase is assumed to be that of water because of the relative low concentration of $NaBH_4$. The heat of vaporization of water is 2250 kJ kg^{-1}. The void fraction of the packed bed is 0.276, and the void fraction of the catalyst pellet is 0.4. The bulk density of the catalyst in the packed bed is 570 kg m^{-3} while the density of the catalyst pellets is 640 kg m^{-3}. The heat of reaction for $NaBH_4$ hydrolysis is $-210{,}000$ kJ kmol^{-1} [19]. We found that $D_{l,A,0} = 8.0 \times 10^{-10}$ m^2 s^{-1} and $k_{H_2O} = 3.0$ m^{-1} produced good fits. This value of $D_{l,A,0}$ is within the typical range of diffusion coefficients for liquids inside catalyst pores [20].

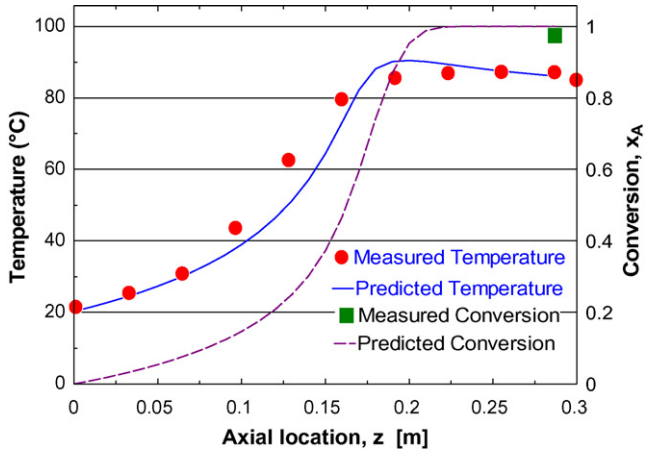

Fig. 4. Axial temperature and conversion profiles ($\dot{m}_{f,0} = 48.5$ g min^{-1}, 10% $NaBH_4$, reference case).

Figs. 4 and 5 present the predicted profiles for temperature, chemical conversion, relative humidity and molar flow rates of hydrogen and water vapor. The temperature increases slowly initially. When it reaches 40 °C, the temperature begins to increase much more rapidly. Chemical conversion follows a similar trend and increases most rapidly when the temperature is between 40 and 85 °C. When chemical conversion approaches 100%, temperature peaks and then begins to decrease as a result of

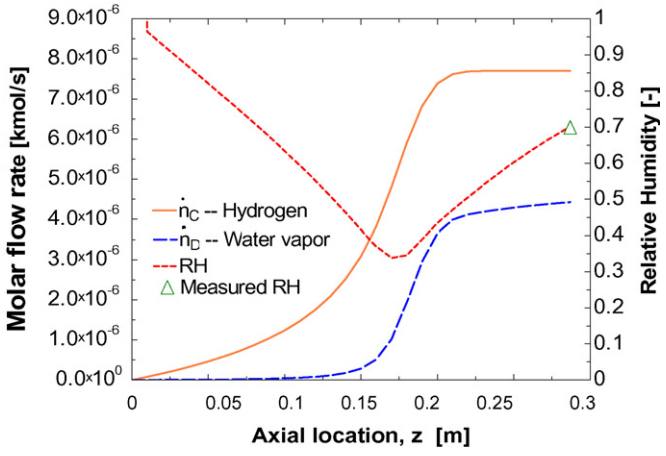

Fig. 5. Axial relative humidity and molar flow rates profiles ($\dot{m}_{f,0} = 48.5$ g min^{-1}, 10% $NaBH_4$, reference case).

evaporative cooling from the mass transfer of liquid water to the hydrogen stream. The profile of molar hydrogen flow rate follows the same trend as chemical conversion, as expected. The profile of molar water vapor flow rate generally follows the conversion trend except near the outlet, where the hydrogen flow rate remains constant and the water vapor flow rate continues to increase because of continuous evaporation of liquid water into the gas stream. Relative humidity initially decreases to a minimum and then begins to increase. The initial decrease in relative humidity is due to the fact that the water vapor added to the hydrogen is insufficient to match the increase in temperature because the temperature and reaction rate are low. The later increase in relative humidity is due to the opposite circumstance, in which the added water vapor to the hydrogen stream, as a result of a much higher reaction rate, is more than enough to match the increase in temperature.

4.2. Model predictions for 10% $NaBH_4$

With $D_{l,A,0}$ and k_{H_2O} obtained at one condition, temperature, chemical conversion, relative humidity and molar flow rates of hydrogen and water vapor profiles for other conditions were calculated and compared to experimental data [3].

4.2.1. Effects of flow rate

Figs. 6–9 show the predictions together with experimental data under different flow rates. The predicted temperature profiles (Figs. 6–8) match experimental data very well, as does the outlet chemical conversion except for the case of $\dot{m}_{f,0} = 64.0\,g\,min^{-1}$ where the predicted chemical conversion exceeds the measurement. The temperature profiles reveal that with increased flow rate, the predicted maximum temperature location (hot-spot) moves downstream, and the rate of conversion decreases because the reaction is highly sensitive to temperature. A relative humidity profile (Fig. 9) is only shown for $\dot{m}_f = 64.0\,g\,min^{-1}$ because only a measurement under this condition was available. The relative humidity was underpredicted, and considering that the experimental uncertainty is approximately ±10%, the agreement in relative humidity is reasonable.

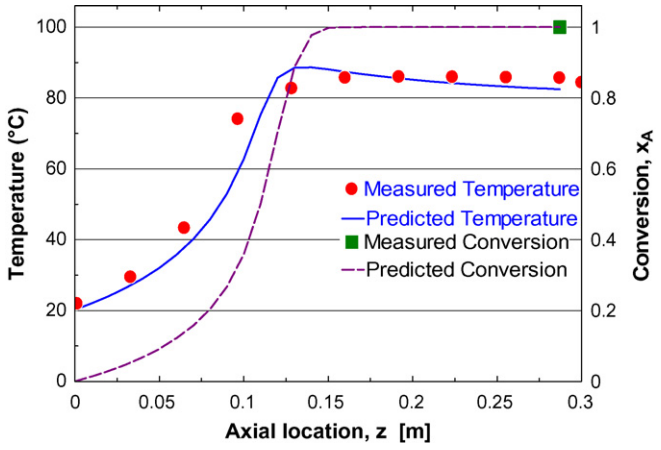

Fig. 7. Axial temperature and conversion profiles ($\dot{m}_{f,0} = 32.5\,g\,min^{-1}$, 10% $NaBH_4$).

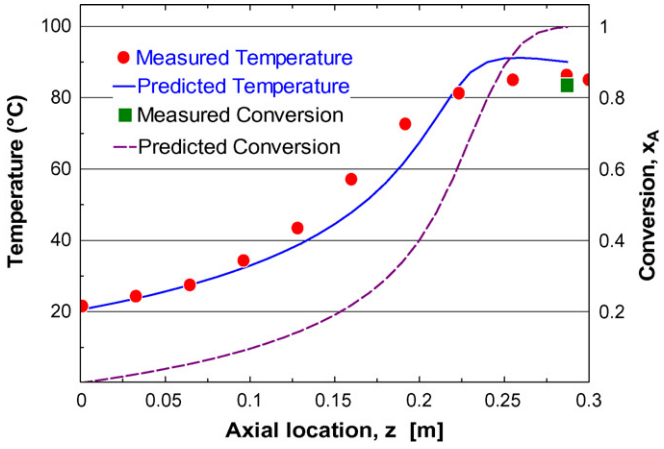

Fig. 8. Axial temperature and conversion profiles ($\dot{m}_{f,0} = 64.0\,g\,min^{-1}$, 10% $NaBH_4$).

4.2.2. Effects of inlet heating

With inlet heating, temperature predictions near the inlet exceed measured temperatures slightly, but the relative humidity at the exit of the reactor matches experimental data very well as depicted in Figs. 10 and 11, respectively. As expected, the

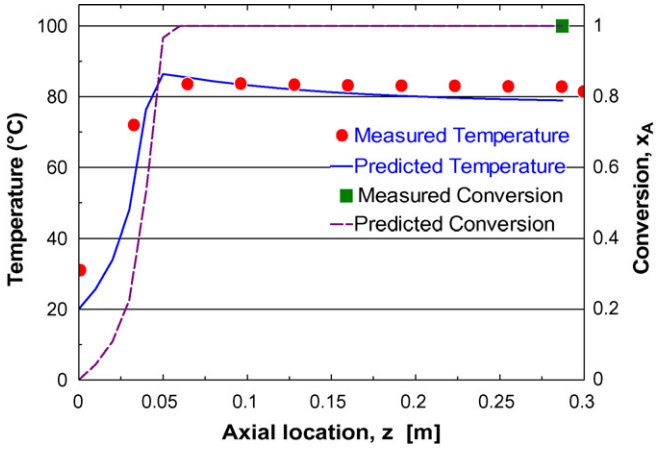

Fig. 6. Axial temperature and conversion profiles ($\dot{m}_{f,0} = 11.5\,g\,min^{-1}$, 10% $NaBH_4$).

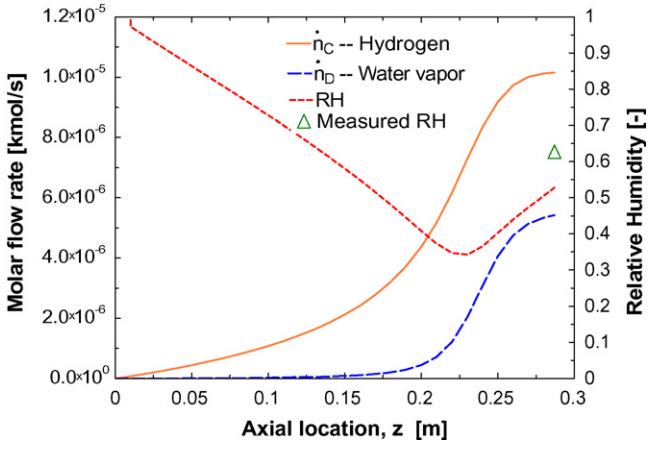

Fig. 9. Axial relative humidity and molar flow rates profiles ($\dot{m}_{f,0} = 64.0\,g\,min^{-1}$, 10% $NaBH_4$).

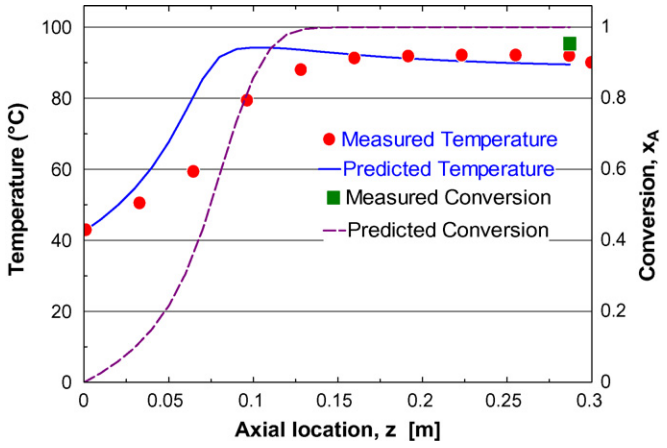

Fig. 10. Axial temperature and conversion profiles ($\dot{m}_{f,0} = 64.0\,g\,min^{-1}$, 10% $NaBH_4$, inlet heating).

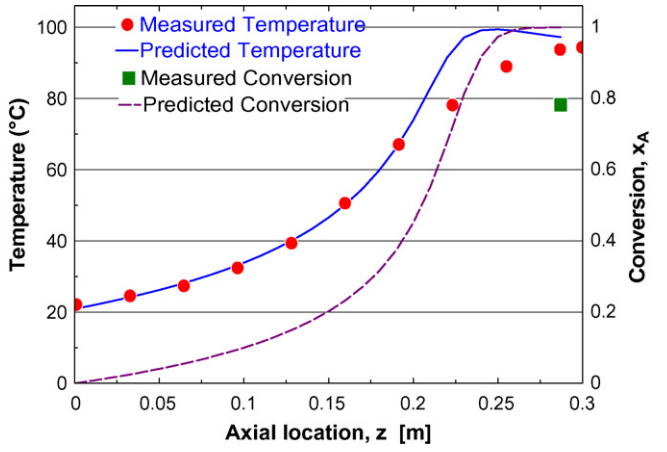

Fig. 12. Axial temperature and conversion profiles ($\dot{m}_{f,0} = 64.0\,g\,min^{-1}$, 10% $NaBH_4$, 13.8 psig system pressure).

relative humidity increased significantly from that in Fig. 9 at the same flow rate but without inlet heating. With inlet heating, the high-temperature portion of the reactor is longer, allowing more time for the transfer of water from the liquid phase to the gas phase while the gas stream passes through the reactor.

4.2.3. *Effects of operation pressure*

Under a higher system pressure condition (Fig. 12), the initial temperature rise is captured well by the model; however, the outlet temperature is overpredicted, as is the chemical conversion primarily due to the overprediction in temperature. Another possible source of discrepancy in chemical conversion is the reduced contact between liquid fuel and catalyst at higher operation pressures as explained in Ref. [3]. This factor is not considered in the current model because the detailed mechanism for reduced contact between liquid fuel and catalyst is still unknown.

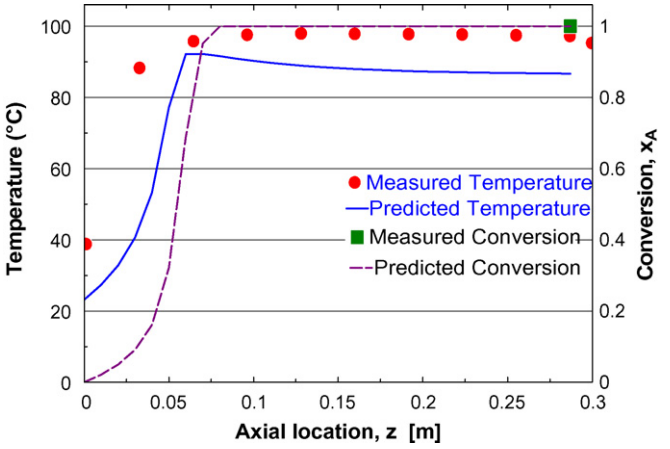

Fig. 13. Axial temperature and conversion profiles ($\dot{m}_{f,0} = 21.7\,g\,min^{-1}$, 15% $NaBH_4$).

4.3. *Model predictions for 15% $NaBH_4$*

Using the same parameters discussed in Section 4.1, the model was used to predict reactor behavior for 15% $NaBH_4$ solution at different flow rates. Because relative humidity was not measured in these tests, only temperature and chemical conversion profiles are presented. At lower flow rates, the model does not capture the initial temperature rise well, as shown in Fig. 13, while at higher flow rates the model captures the initial temperature rise very well, as shown in Fig. 14. As discussed in

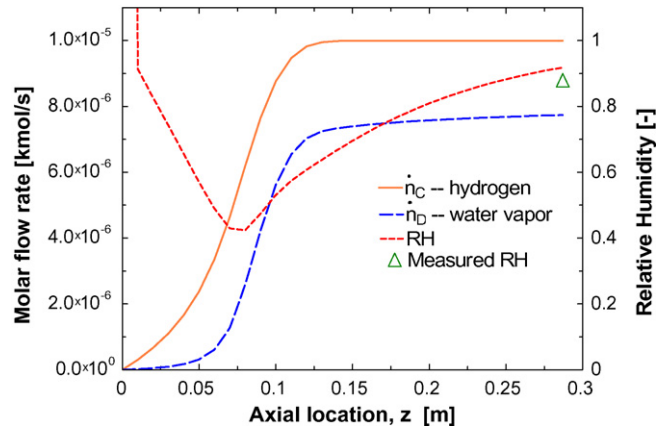

Fig. 11. Axial relative humidity and molar flow rates profiles ($\dot{m}_{f,0} = 64.0\,g\,min^{-1}$, 10% $NaBH_4$, inlet heating).

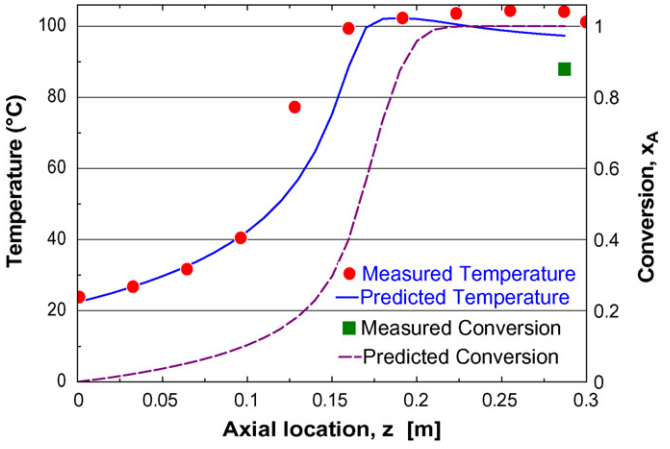

Fig. 14. Axial temperature and conversion profiles ($\dot{m}_{f,0} = 64.3\,g\,min^{-1}$, 15% $NaBH_4$).

Table 2
Comparison of predicted pressure drops with experimental data (10% $NaBH_4$)

	$\dot{m}_f$ (g min^{-1})						
	11.5	32.5	48.5	64.0	64.0, inlet heating	64.0, 9.6 psig	64.0, 13.8 psig
Measured ΔP (psi)	0.8	2.0	3.0	3.2	4.3	2.4	1.8
Predicted ΔP (psi)	0.90	2.2	3.0	3.2	6.3	2.9	2.8

Ref. [3], the initial temperature rise was very different for flow rates below 35 g min^{-1} than for flow rates above 35 g min^{-1}. For flow rates below 35 g min^{-1}, the rapid temperature rise may be partially due to axial heat conduction from downstream to upstream. The entry temperature increases to approximately 40 °C (Fig. 13) while the fuel's initial temperature is only 22 °C. With an increased fuel flow rate, the effects of heat conduction are reduced, and the model predictions agree with experimental data. Temperatures near the exit of the reactor are underpredicted for all cases, presumably because of overestimated water evaporation into the hydrogen stream passing through the reactor. A smaller value of k_{H_2O} may mitigate this situation. Further, using a smaller k_{H_2O} may be consistent with the experimental process because at higher $NaBH_4$ or $NaBO_2$ concentrations, water is less likely to evaporate than it is at lower concentrations [21]. The chemical conversion predictions match experimental data well for flow rates up to 53.2 g min^{-1}. At the higher flow rate of 64.3 g min^{-1}, chemical conversion is slightly overpredicted.

4.4. Prediction of pressure drop

The predicted pressure drops across the reactor are compared to experimental data in Table 2. Only experiments with 10% $NaBH_4$ are considered. At 15% $NaBH_4$ concentration, the viscosity of the discharge stream increases significantly as explained in reference [3], and the pressure characteristics change dramatically. The pressure drop predictions are excellent, especially for different flow rates. The predicted pressure drop under the inlet heating condition exceeds the measurement, perhaps due to the overpredicted initial temperature rise discussed in Section 4.2.2. For pressurized conditions, the pressure drop is also overestimated, perhaps due to the discrepancies in chemical conversion. However, the trend of decreasing pressure drop at higher system pressures was captured by the present model. Decreased pressure drop is likely due to lower water vaporization rates inside the reactor at higher operating pressures.

4.5. Recommendations

Both the previous experimental study [3] and present modeling results reveal that inlet heating can significantly increase reaction rates in the entry section of the reactor and increase the overall chemical conversion at high flow rates. Inlet heating (e.g., via exhaust recirculation) could be adopted to reduce the length of the reactor and the amount of catalyst used. Further, temperature measurements could prove to be effective in real-time performance (conversion) monitoring. The effects of operation pressure on overall chemical conversion were inconsistent between experimental study and modeling results, and further investigation of this issue is warranted.

5. Conclusions

A one-dimensional/homogeneous catalyst distribution model has been developed to simulate thermo-chemical processes inside a $NaBH_4$ hydrolysis packed bed reactor. The model successfully captures water vapor generation both by chemical reactions and by mass transfer from the liquid phase to the gas phase. The pressure drop has been calculated based on two-phase flow and porous media theories. The overall model has been used to predict reactor behavior at different fuel concentrations, flow rates and reactor pressures. The predicted temperature profiles, fuel conversion and relative humidity compare reasonably well to experimental data. The predicted pressure drops also match experimental data very well at different flow rates, although pressure drops under pressurized and inlet heating conditions are overpredicted. Considering the complexity of processes occurring inside the reactor, the present results are encouraging. The numerical model is based on fundamental heat and mass transfer and chemical kinetics theories; therefore it is expected to be useful in studying and optimizing hydrogen storage systems using $NaBH_4$ and other chemical hydrides.

Acknowledgements

The authors thank General Motors and the Energy Center at Discovery Park of Purdue University for the financial supports. We also thank Prof. Nick Delgass in Purdue's School of Chemical Engineering for insightful discussions.

References

[1] S.C. Amendola, S.L. Sharp-Goldman, M.S. Janjua, M.T. Kelly, P.J. Petillo, M. Binder, J. Power Sources 85 (2000) 186–189.
[2] J.S. Zhang, W.N. Delgass, T.S. Fisher, J.P. Gore, J. Power Sources 164 (2007) 772–781.
[3] J.S. Zhang, Y. Zheng, J.P. Gore, T.S. Fisher, 1 kW_e sodium borohydride hydrogen generation system, Part I: Experimental Study, J. Power Sources 165 (2007) 844–853.
[4] S.A. Shah, Chemical hydride based PEM fuel cells for portable power applications, in: Proceedings of Joint Services Power Expo, Tampa, FL, May 2–5, 2005.
[5] S. Suda, in: W. Vielstich, H.A. Gasteiger, A. Lamm (Eds.), Handbook of Fuel Cells—Fundamentals, Technology and Applications, John Wiley & Sons, Hoboken, NJ, 2003, pp. 115–120.
[6] J.S. Zhang, Thermal Processes of Sodium Borohydride Hydrogen Storage Systems, Ph.D. Thesis, Purdue University, West Lafayette, IN, 2006.
[7] R.M. Mohring, R.E. Luzader, SAE paper 2001-01-2529.

[8] G.F. Froment, K.B. Bischoff, Chemical Reactor Analysis and Design, John Wiley & Sons, New York, 1990.
[9] F.P. Incropera, D.P. DeWitt, Fundamentals of Heat and Mass Transfer, John Wiley & Sons, New York, 1996.
[10] L.S. Tong, Y.S. Tang, Boiling Heat Transfer and Two-phase Flow, Taylor & Francis, Washington, DC, 1997.
[11] H.S. Fogler, Elements of Chemical Reaction Engineering, Prentice Hall PTR, New Jersey, 1999.
[12] G.W. Roberts, C.N. Satterfield, Ind. Eng. Chem. Fundam. 4 (1965) 288–326.
[13] G.W. Roberts, C.N. Satterfield, Ind. Eng. Chem. Fundam. 5 (1966) 317–324.
[14] C.W. Knudsen, G.W. Roberts, C.N. Satterfield, Ind. Eng. Chem. Fundam. 5 (1966) 325–326.
[15] J.H. Hong, W.C. Hecker, T.H. Fletcher, Energy Fuels 14 (2000) 663–670.
[16] C.N. Satterfield, Mass Transfer in Heterogeneous Catalysis, MIT Press, Cambridge, MA, 1970.
[17] P.N. Dwidevi, S.N. Upadhyay, Ind. Eng. Chem. Process Des. Dev. 16 (1977) 157–165.
[18] Engineering Equation Solver (EES), 2006. http://www.fchart.com/ees/ees.shtml.
[19] J.S. Zhang, T.S. Fisher, J.P. Gore, D. Hazra, P.V. Ramachandran, Int. J. Hydrogen Energy 31 (2006) 2292–2298.
[20] P.B. Weisz, Chem. Eng. Prog. Symp. Ser. 25 (1959) 29–36.
[21] D.D. Ebbing, General Chemistry, third ed., Houghton Mifflin, Boston, MA, 1990.